

Magnetic gap opening in rhombohedral-stacked multilayer graphene from first principles

Betül Pamuk,¹ Jacopo Baima,¹ Francesco Mauri,^{2,3,*} and Matteo Calandra^{1,†}

¹*CNRS, UMR 7590 and Sorbonne Universités, UPMC Univ Paris 06, IMPMC - Institut de Minéralogie, de Physique des Matériaux, et de Cosmochimie, 4 place Jussieu, F-75005, Paris, France*

²*Dipartimento di Fisica, Università di Roma La Sapienza, Piazzale Aldo Moro 5, I-00185 Roma, Italy*

³*Graphene Labs, Fondazione Istituto Italiano di Tecnologia, Via Morego, I-16163 Genova, Italy*

(Dated: April 30, 2019)

We investigate the occurrence of magnetic and charge density wave instabilities in rhombohedral-stacked multilayer (three to eight layers) graphene by first principles calculations including exact exchange. Neglecting spin-polarization, an extremely flat surface band centered at the special point \mathbf{K} of the Brillouin zone occurs at the Fermi level. Spin polarization opens a gap in the surface state by stabilizing an antiferromagnetic state. The top and the bottom surface layers are weakly ferrimagnetic in-plane (net magnetization smaller than $10^{-3} \mu_B$), and are antiferromagnetic coupled to each other. This coupling is propagated by the out-of-plane antiferromagnetic coupling between the nearest neighbors. The gap is very small in a spin-polarized generalized gradient approximation, while it is proportional to the amount of exact exchange in hybrid functionals. For trilayer rhombohedral graphene it is 38.6 meV in PBE0, in agreement with the 42 meV gap found in experiments. We study the temperature and doping dependence of the magnetic gap. At electron doping of $n \sim 7 \times 10^{11} \text{ cm}^{-2}$ the gap closes. Charge density wave instabilities with $\sqrt{3} \times \sqrt{3}$ periodicity do not occur.

In a solid, at low enough density, the Coulomb energy dominates the single particle energy and electronic instabilities such as magnetic phases or even Wigner crystallization become possible. A reduction of the single-particle energy, and a consequent enhancement of the electron-electron interaction, can be obtained by considering a metallic system with a very flat single-particle band-dispersion. This unfortunately does not happen in graphene where the high Fermi velocity prevents electronic instability. The situation is different, however, in weakly doped Bernal-stacked (AB) even-multilayer graphene (see Fig. 1), as the single-particle bands become massive. Indeed, a spontaneously gapped ground state is already observed in suspended bilayer^{1,2} and four-layer graphene (1.5 meV gap)³.

Even more favorable to electronic instabilities is rhombohedral-stacked (ABC) multilayer graphene. Neglecting spin polarization, tight-binding and density functional theory (DFT) calculations find bulk rhombohedral graphite to be metallic with a high Fermi velocity (see grey region in Fig. 1). On the contrary, within these approximations, rhombohedral-stacked multilayer graphene (RSMG) displays the occurrence of an extremely flat surface state at the Fermi level (see Fig. 1) located at the \mathbf{K} point of the graphene Brillouin zone (BZ)⁴⁻⁹. The extension of the surface state in the BZ increases with increasing thickness and saturates at ≈ 7 layers. Its bandwidth is at most 2 meV for flakes of fewer than eight layers. The extremely reduced bandwidth makes RSMG one of the strongest correlated systems known nowadays and an ideal candidate for correlated states even in the absence of d orbitals.

On the experimental side, only recently has it been possible to synthesize RSMG. Ouerghi *et al.*¹⁰ found five-

layer RSMG on top of a cubic SiC substrate to be metallic with a very high density of states at the Fermi level, in agreement with spinless DFT predictions. More recent work on suspended ABC trilayer¹¹ seems to suggest that a gap as large as 42 meV occurs at the Fermi level. However, in transport measurements with singly gated devices, where the charge density and the potential difference cannot be controlled independently, the gap is much smaller¹². The origin of this gap state has been suggested to be related to a magnetic state in which the external layers are antiferromagnetic coupled while the in-plane spin state is ferrimagnetic^{11,13}. Finally, it is worth mentioning that it has been claimed that RSMG flakes composed of 17 layers can be isolated from kish graphite¹⁴. However it is still unknown if a gap opens in these samples.

In this work, by using density functional theory calculations with several hybrid functionals we investigate the occurrence of charge and magnetic instabilities in RSMG. We also discuss the effect of doping and temperature on the interaction induced gap.

DFT calculations are performed using the CRYSTAL code¹⁵ with the triple- ζ -polarized Gaussian type basis sets for the C atoms¹⁶. The PBE0¹⁷ and other hybrid functionals with several degrees of exact exchange (see Appendix A) have been used for DFT calculations. The band flatness and the extreme localization of the low energy states around the special point \mathbf{K} require an ultra-dense sampling with an electronic k mesh of $516 \times 516 \times 1$. We used real space integration tolerances of 7-7-7-15-30, and with an energy tolerance of 10^{-11} Ha for the total energy convergence. Fermi-Dirac smearing for the occupation of the electronic states is used for all of the calculations. The density of states is obtained with a Gaussian

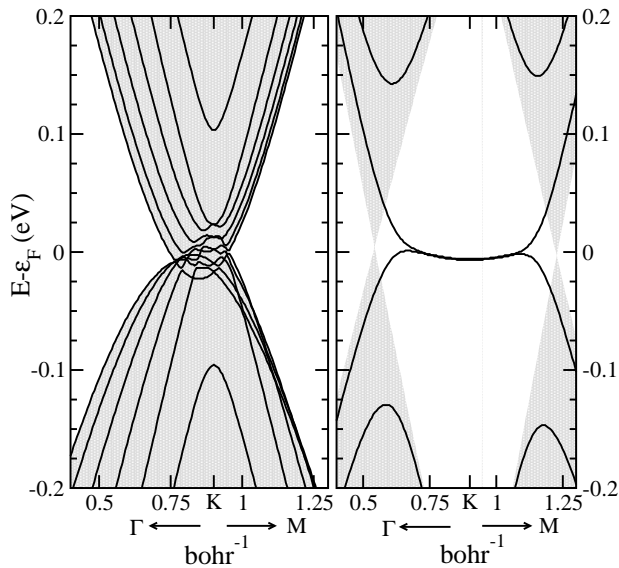


FIG. 1. Electronic structure (black lines) of a 10-layer Bernal (left) and rhombohedral (right) -stacked multilayer graphene calculated with the LDA functional. The gray regions are the bulk electronic structures projected over the surface.

smearing of 0.00005 Ha. In the magnetic case, we fix the magnetic state in the first iteration of the self-consistent cycle and then we release the constraint. We choose an in-plane lattice parameter of $a = 2.461 \text{ \AA}$, and an inter-plane distance of 3.347 \AA . A vacuum of 10.04 \AA is placed between the periodic images along the z direction.

We consider $N \geq 3$, N being the number of layers. We start the simulation from an initial magnetic state having ferromagnetic coupling in the surface layers and antiferromagnetic coupling between them. In both spin polarized PBE¹⁸ and exact exchange functionals (HSE06, PBE0, etc.), we always converge to a magnetic state that is (1) globally, an antiferromagnetic spin state, namely for each spin up band we have a spin down band degenerate in energy but localized on different atoms; (2) ferrimagnetic within the surface layers where the two atoms have opposite spins with slightly different magnetic moment; and (3) with antiferromagnetic coupling between the top and bottom layers. The magnitude of the spin drops significantly farther away from the surface. This magnetic state is similar to the one found in bilayer and trilayer graphene in the framework of Hubbard-like models^{11,13} (the so-called layered antiferromagnetic state); however, here the module of the magnetic moments in each outer surface layer is identical up to $0.001 \mu_B$, meaning that we are much closer to an in-plane antiferromagnetic state than a ferrimagnetic state.

Figure 2 shows a schematic diagram of rhombohedral graphene, with arrows representing the direction of the spin for all layers up to eight layers. In rhombohedral graphene, the total number of atoms is $N_{\text{atom}} = N$, with each layer having two covalent bonded C atoms, only

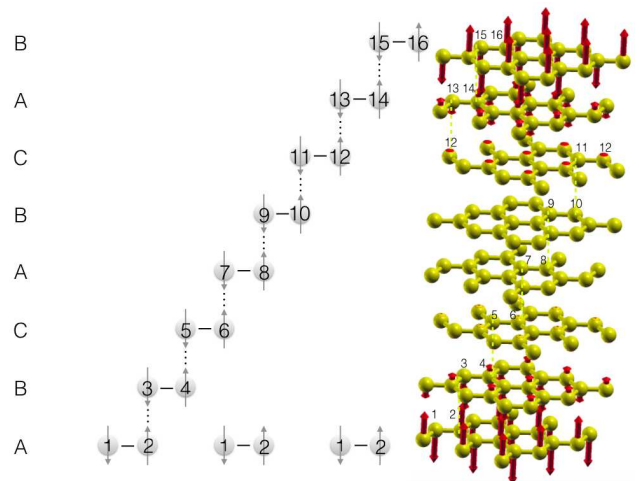


FIG. 2. Left: Schematic of the rhombohedral graphene with ABC stacking sequence. Solid lines represent the in-plane covalent bond, and dashed lines represent the out-of-plane weak interlayer bond. The arrows represent only the direction of the spin, as the magnitude is layer dependent. Right: The atomic structure of rhombohedral eight-layer graphene.

one of which is weakly bonded to the neighboring layer. The labeling of the atoms starts from the bottom layer, where atom 1 is covalent bonded to atom 2, and atom 2 is weakly bonded to atom 3 of the next layer, and the labeling follows the covalent to weak interlayer bond. The magnetic order we find is such that the odd-numbered atoms have up spin, and the even numbered atoms have up spin, with the spin magnetic moments such that $\mu_i = -\mu_{N_{\text{atom}}-i+1}$. The outermost surface layers are ferrimagnetic with $\mu_1 > \mu_2$. In-plane and out-of-plane nearest neighbors are antiferromagnetic coupled.

Within spin-polarized PBE, the local magnetic moments are essentially zero. The increase of the exact exchange component in the functional enhances the magnetic moments. The magnetic moments in the outermost layers are larger for eight-layer thick flakes and within PBE0 they are as large as 10^{-2} bohr magnetons in magnitude (see Table I). The magnetic moments for other functionals are shown in Appendix A.

The PBE0 magnetic electronic structure for $3 \leq N \leq 8$ is shown in Fig. 3. Each band is doubly degenerate with spin up and down states having the same energy. Therefore globally the system is in an antiferromagnetic state. This magnetic order results in a gapped state, with the gap at the \mathbf{K} point increasing with N . The surface bands are quite flat with a small asymmetry between the $\mathbf{\Gamma} \rightarrow \mathbf{K}$ and $\mathbf{K} \rightarrow \mathbf{M}$ directions that increases with N . This behavior is easily understood as for $N \rightarrow \infty$ the surface projected bulk bands of rhombohedral graphite should be recovered (see Fig. 1). More insight into the gap opening at \mathbf{K} is obtained by analyzing the projected electronic bands on the atoms of the surface layers. The surface states are dominated by the p_z orbitals of two C atoms. On each surface layer, only the atom having no

TABLE I. The magnitude of the spin of each atom in $10^{-3}\mu_B$ for rhombohedral N -layer graphene. The spins are reported up to $\mu_{N_{\text{atom}}/2}$, and the spins of the rest of the atoms, as well as the direction of the spin can be obtained by $\mu_i = -\mu_{N_{\text{atom}}-i+1}$. This direction can be matched to Fig. 2.

N	$\mu_1 = -\mu_{N_{\text{atom}}}$	μ_2	μ_3	μ_4	μ_5	μ_6	μ_7	μ_8
3	-5.28	4.60	-2.73					
4	-7.32	6.33	-3.22	3.11				
5	-8.56	7.38	-3.62	3.43	-2.60			
6	-9.19	7.90	-3.82	3.58	-2.34	2.29		
7	-9.75	8.40	-4.11	3.84	-2.38	2.30	-1.93	
8	-10.04	8.64	-4.23	3.94	-2.34	2.24	-1.69	1.66

out-of-plane neighboring atoms contributes to the surface bands (see Appendix B). For comparison, the electronic structure of metallic and paramagnetic state is given Appendix C.

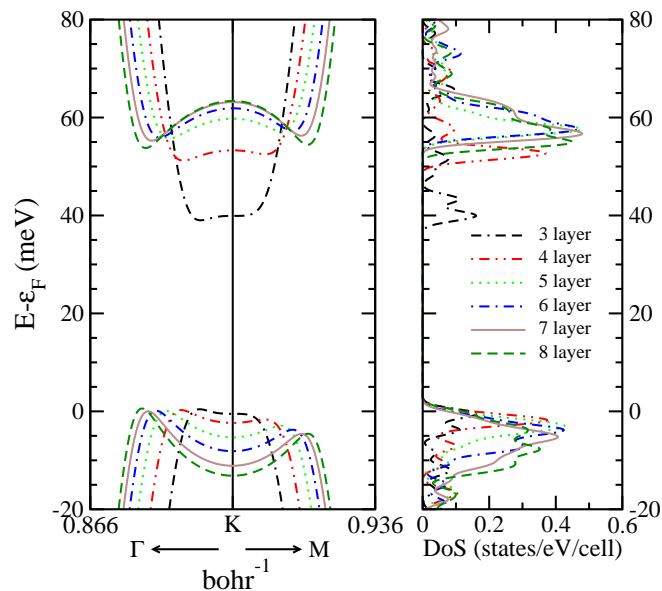


FIG. 3. The electronic band structure (left) and density of states (right) of the surface states of the magnetic state of the rhombohedral graphene up to eight layers calculated with the PBE0 functional. The electronic bands are plotted around 0.035 bohr^{-1} of the \mathbf{K} point along the path $\Gamma \rightarrow \mathbf{K} \rightarrow \mathbf{M}$, and each band is spin degenerate.

We find the band gap for rhombohedral trilayer graphene to be $E_g = 38.6 \text{ meV}$ with the PBE0 functional. This result is in good agreement with the experimentally reported value of $E_g = 42 \text{ meV}$ in Ref.¹¹. By using other functionals with different percentages of exact exchange and range separation we find smaller gaps as shown in Appendix A. As the PBE0 gap gives the best agreement with experiment we use this functional for the rest of the paper.

The change in the band gap at zero temperature for different layers is shown in Figs. 3 and 4 and Table II. The band gap increases significantly from three to four layers, but saturates after five layers. At eight layers, the

gap starts to close slowly, with increasing deviation from the flat bands, in order to reach the bulk limit¹⁹ shown in Fig. 1.

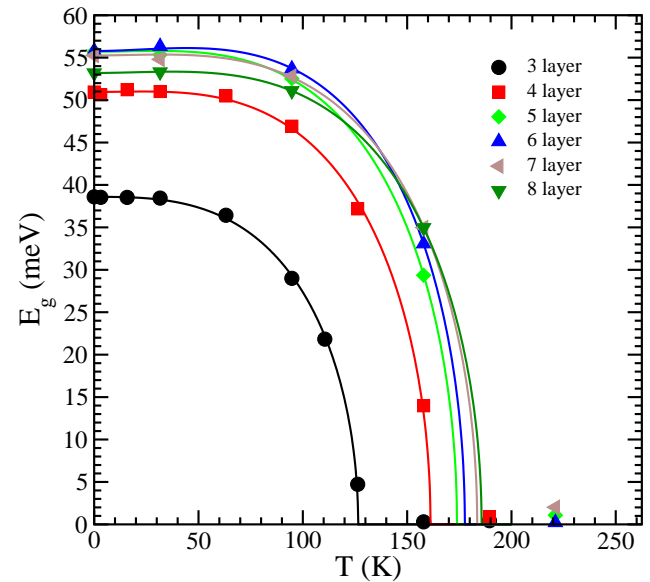


FIG. 4. Temperature dependence of the band gap, E_g , up to eight layers. The dots are the data obtained with PBE0 functional. The lines are the result of the fit to eq. (1).

As the gap is strongly temperature dependent in experiments and closes at $T_c = 34 \text{ K}$ ¹¹, we study the antiferromagnetic gap as a function of temperature. This is done by including a Fermi-Dirac occupation of the electronic states. The temperature dependence of the gap is shown in Fig. 4. To obtain T_c , we fit the band gap to the function,

$$E_g(T) = E_g(0) \left[A \left(1 - \frac{T}{T_c} \right) + (3 - 2A) \left(1 - \frac{T}{T_c} \right)^2 + (A - 2) \left(1 - \frac{T}{T_c} \right)^3 \right]^{1/2} \quad (1)$$

with the constants arranged such that the first and the second derivative of the curve is zero at the zero temperature limit. The temperature dependence of the band

gap has a similar behavior to that obtained from the experiments in Ref.¹¹. However, the thermal suppression of the gap is slower in our calculations, resulting in a larger $T_c = 126.5$ K, as compared to the experimental value of $T_c = 34$ K for trilayer graphene. We attribute the discrepancy between theory and experiments to the imperfect treatment of screening at the hybrid functional level.

Similarly to what happens for the layer dependence of the band gap with the number of layers, T_c increases up to five layers, and then saturates and changes slowly. The T_c values and the fit parameter A of each layer are shown in Table II for different numbers of layers.

TABLE II. The T_c values and the fit parameter A of eq. (1) of each layer.

N	$E_g(0)$ (meV)	T_c (K)	A
3	38.60	126.53	2.97
4	50.96	161.21	3.28
5	55.70	173.90	3.36
6	55.78	177.67	3.60
7	55.26	183.58	3.36
8	53.19	185.67	3.43

Contrary to the case of suspended samples, supported RSMG shows a metallic behavior¹⁰. A possible reason for this could be the presence of a substrate doping¹¹. In order to verify this hypothesis, we consider n-doping of rhombohedral trilayer graphene. We use a compensating jellium background to enforce charge neutrality.

To estimate the number of electrons needed to close the gap, we have integrated the first peak of the density of states in Fig. 3. For the trilayer rhombohedral graphene an electron density of $n = 8.01 \times 10^{11} \text{ cm}^{-2}$ (corresponding to $x = 0.00042$ electrons/cell) is needed to fill the flat conduction band region. This electron density increases to $n = 67.70 \times 10^{11} \text{ cm}^{-2}$ for eight layers. The results for the rest of the layers are presented in Appendix D.

We find that doping reduces the band gap. In agreement with our estimation from the density of states, the gap ultimately closes at $n \sim 7 \times 10^{11} \text{ cm}^{-2}$, to be compared to $n \sim 3 \times 10^{11} \text{ cm}^{-2}$ found in experiments¹¹. The combined effect of doping and temperature is shown in Fig. 5 (and in Appendix E). We conclude that substrate doping can be responsible of the differences between supported and suspended samples. We can also speculate that the critical doping to close the gap could grow by an order of magnitude by increasing the number of ABC stacked layers.

Up to now we consider the possibility of magnetic gap opening in RSMG. However, charge density wave instabilities could also open a gap via phonon softening. In order to validate this hypothesis, we calculate phonon frequencies at Γ and \mathbf{K} by using the finite differences method and the spinless PBE0 functional in rhombohedral-stacked trilayer graphene. We find that the largest softening occurs at the \mathbf{K} point of the Brillouin zone²⁰ for the in-plane phonon mode. Despite

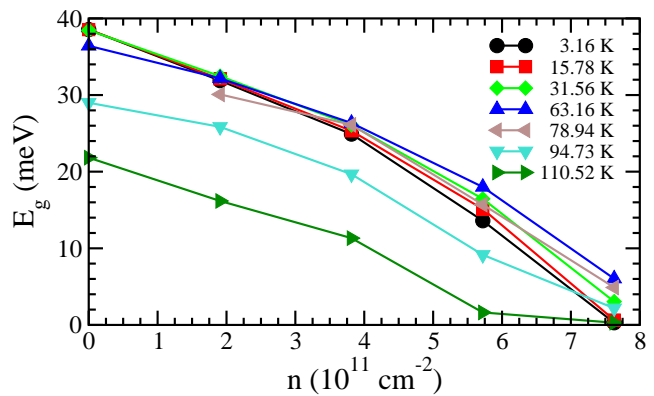


FIG. 5. Doping dependence of the band gap of rhombohedral trilayer graphene at different temperatures. The lines are to guide the eye.

PBE0 substantially softens the phonon frequencies with respect to PBE, all the phonon modes are stable so that a structural distortion compatible with a $\sqrt{3} \times \sqrt{3}$ periodicity is excluded. The magnitude of the phonon modes are also reported in Appendix F. Magnetism is then the most likely instability in RSMG.

In this paper, we have analyzed the magnetic and charge instabilities in rhombohedral stacked multilayer graphene using spin-polarized hybrid functionals. While in the absence of spin-polarization an extremely flat surface state occurs at the Fermi level, the introduction of spin polarization leads to magnetic instabilities and opening of a gap in the surface state. The state is such that the surface layers are weakly ferrimagnetic in-plane, and the top and the bottom layers are antiferromagnetic coupled, which is propagated by the out-of-plane antiferromagnetic coupling between the nearest neighboring atoms. The globally stable state is antiferromagnetic where the spin up and spin down bands are degenerate. Within PBE0 the gap is found to agree with experiments on ABC trilayer graphene. We have shown that doping suppresses the gap, explaining the experimental finding that a gap occurs in trilayer ABC graphene only in suspended samples. Finally, we study the possible occurrence of charge density wave instabilities with $\sqrt{3} \times \sqrt{3}$ supercell. We found that no charge density wave occurs so that the gap opening seen in experiments is only due to the magnetic coupling of the surface atoms in the multilayers. Our work demonstrates that the inclusion of exact exchange in first principles calculations and an ultradense sampling of the Brillouin zone are crucial in order to explain the magnetic and structural instabilities of rhombohedral-stacked multilayer graphene.

ACKNOWLEDGMENTS

This work is supported by the Graphene Flagship, and by Prace (Proposal number 2015133134). Calculations were performed at IDRIS, CINES, CEA and BSC TGCC.

Appendix A: Exchange and Correlation Functionals

To understand the effect of exchange and range separation in the hybrid functionals on the band gap of the system, we have tuned exchange components and range separation. The results are given in Fig. 6.

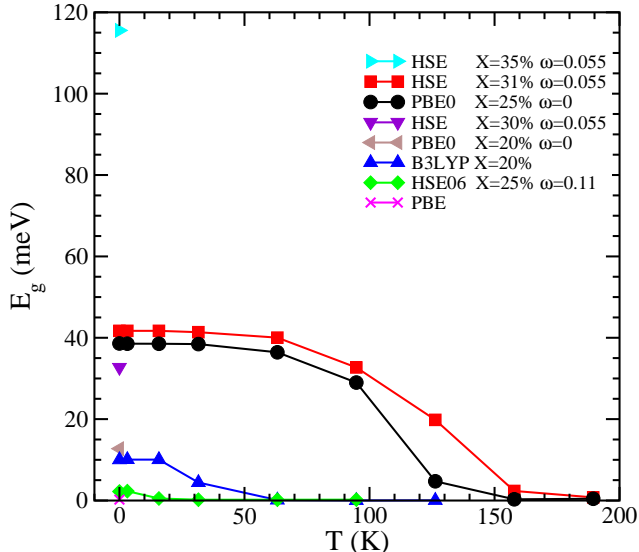


FIG. 6. Change in the band gap with different DFT functionals with different exact exchange (X) percentage (%) and range separation (ω) in \AA^{-1} for rhombohedral trilayer graphene. The lines are to guide the eye.

For the same range separation parameter, $\omega = 0.055 \text{\AA}^{-1}$, the increasing percentage of exact exchange increases the band gap significantly. For the same percentage of exact exchange, increasing the range separation decreases the band gap, as can be seen when comparing the PBE0 functional to the HSE06 functional²¹.

Only with PBE0 functional, we obtain a band gap similar to the experimental value.

When we change the exact exchange and range separation of the HSE functional such that the band gap is similar to that of PBE0 at zero temperature limit ($X = 31\%$, $\omega = 0.055 \text{\AA}^{-1}$), we obtain a similar temperature dependence for both functionals.

With the B3LYP functional²², we obtain a T_c similar to the experimental value, however the calculated band gap at zero temperature is too small compared to the experimental result¹¹.

The value of the band gap is directly linked to the magnitude of the spin in the surface atoms, which can be seen in Table III. The PBE functional predicts a spinless paramagnetic state, while the introduction of the exact exchange immediately stabilizes the magnetic state. With the increase of the amount of exact exchange the magnitude of the spin on the surface atoms increases, and with the increase of the range separation the magnitude of the spin of the surface atoms decreases.

TABLE III. The magnitude of the spin of each atom in $10^{-3}\mu_B$ at $T = 0 \text{ K}$ for rhombohedral trilayer graphene calculated by different exchange and correlation functionals (XC) with different exact exchange (X) percentage (%) and range separation (ω) in \AA^{-1} .

XC	X	ω	$\mu_1 = -\mu_6$	$\mu_2 = -\mu_5$	$\mu_3 = -\mu_4$
PBE	0	0	-0.0001	0.0001	-0.0002
HSE06	25	0.11	-0.4589	0.3581	-0.1282
B3LYP	20	0	-1.4442	1.1316	-0.5043
PBE0	20	0	-1.8892	1.5258	-0.7099
HSE	30	0.055	-5.2116	4.5689	-2.6368
PBE0	25	0	-5.2831	4.5951	-2.7317
HSE	31	0.055	-6.5798	5.8432	-3.5352
HSE	35	0.055	-17.5428	16.2741	-12.3476

Appendix B: Projected Band Structure

In Fig. 7, we present the electronic band structure projected onto the spin-down state of p_z orbital. The flat bands are dominated by atom 1 (blue in the figure) and 6 (green), for the spin down bands. These are one of the atoms on each surface, and are antiferromagnetic coupled. The other atom of each surface, i.e., atoms 2 and 5 (red), contribute only to the bulk bands. The spin-up figure would look exactly the same except now blue would be atom 6 and green would be atom 1.

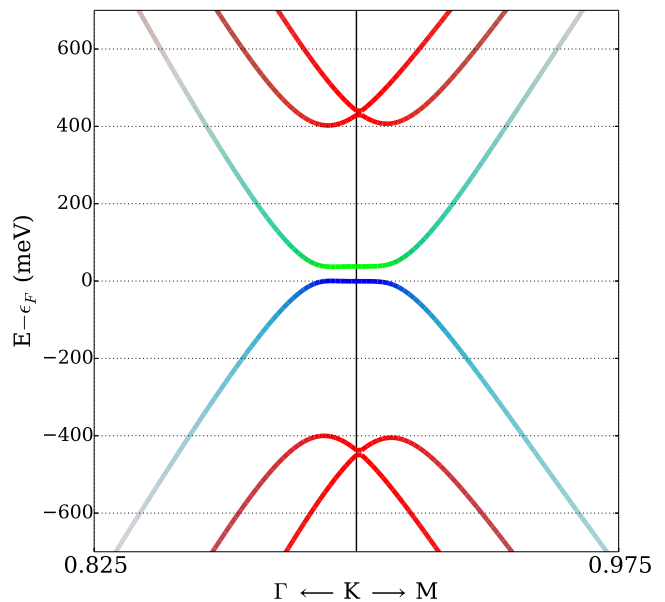


FIG. 7. The electronic band structure of trilayer rhombohedral graphene projected onto p_z orbital spin-down state of atom 1 (blue), 6 (green), and 2 and 5 combined (red). The electronic bands are plotted around 0.075 bohr^{-1} of the \mathbf{K} point along the path $\Gamma \rightarrow \mathbf{K} \rightarrow \mathbf{M}$.

In order to understand the interplay between in-plane and out-of-plane magnetic couplings in determining the gap structure we performed, for three and four layers, a calculation starting from an in-plane antiferromagnetic

spin order and an out-of-plane ferromagnetic order. The self-consistent cycle preserves this magnetic state; however, the resulting band structure is gapless. This reveals that the inter-layer antiferromagnetic coupling plays a crucial role in the gap opening in three- and four-layer rhombohedral graphene.

Appendix C: Metallic and Paramagnetic Bands

In Fig. 8, we present the electronic band structure and the density of states of the paramagnetic state calculated with the PBE0 functional between three and eight layers.

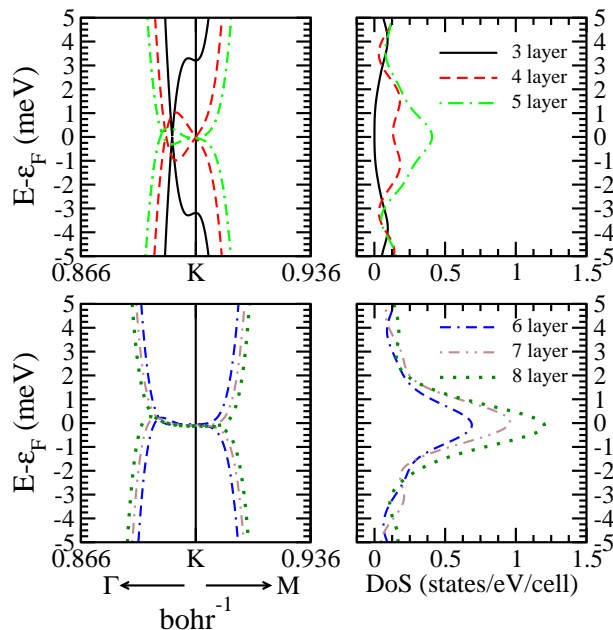


FIG. 8. The electronic band structure (left) and density of states (right) of the surface states of the paramagnetic state of the rhombohedral graphene up to eight layers. The electronic bands are plotted around 0.035 bohr^{-1} of the \mathbf{K} point along the path $\Gamma \rightarrow \mathbf{K} \rightarrow \mathbf{M}$.

The paramagnetic electronic band calculations are performed with the same parameters as the magnetic calculations, except the initial conditions on the spin of each atom are not set and Fermi-Dirac smearing of 0.00001 Ha is used. The density of states is calculated with a Gaussian smearing of 0.00004 Ha .

The crossing points of the bands in our paramagnetic calculations are comparable to the previous results obtained for three and four layers with standard DFT calculations⁶.

As compared to the bulk bands of rhombohedral graphite with DFT^{7,23–25} and tight binding²⁵ calculations, and to the evolution of graphene to graphite with tight binding calculation¹⁹, it is clear that these states are surface states of the few-layer rhombohedral graphene.

Appendix D: Electrons on the Flat Surface Bands

In order to understand the amount of charge needed to fill the flat surface band and close the gap, we have integrated first peak of the density of states above the gap. The results for each layer are shown in Table IV.

TABLE IV. The number of electrons, x , in units of electrons/cell and the electron density, n , in units of 10^{11} cm^{-2} , needed to fill the flat surface bands, for each layer.

N	x	n
3	0.00042	8.01
4	0.00116	22.12
5	0.00209	39.86
6	0.00268	47.30
7	0.00326	62.17
8	0.00355	67.70

For the trilayer rhombohedral graphene, a doping of $x = 0.00042$ electrons/cell is needed to fill the flat conduction band, and this is in agreement with our calculations that at ~ 0.0004 electrons/cell the band gap closes, as will be discussed in the following Appendix. Note that the width of the flat region decreases with increasing doping.

Appendix E: Band Gap with Changing Temperature and Doping

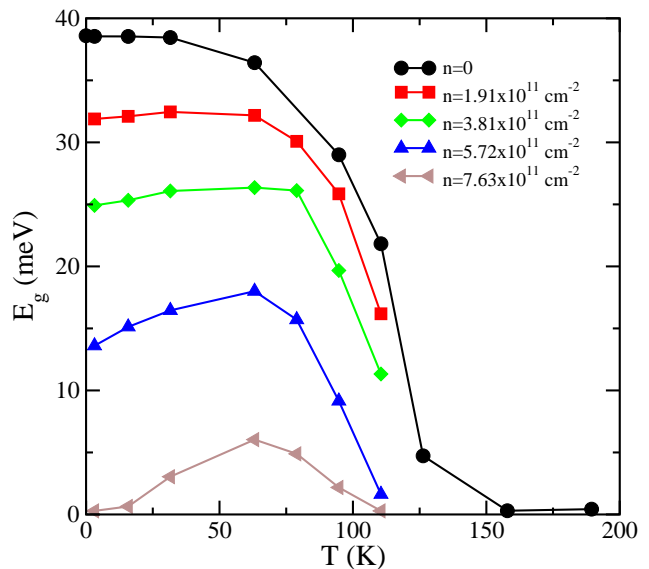


FIG. 9. Temperature dependence of the band gap for rhombohedral trilayer graphene with different doping. The dots are the data obtained with PBE0 functional. The lines are to guide the eye.

To understand the effect of the doping on the band gap, we introduced $x = 0.0001, 0.0002, 0.0003, 0.0004$

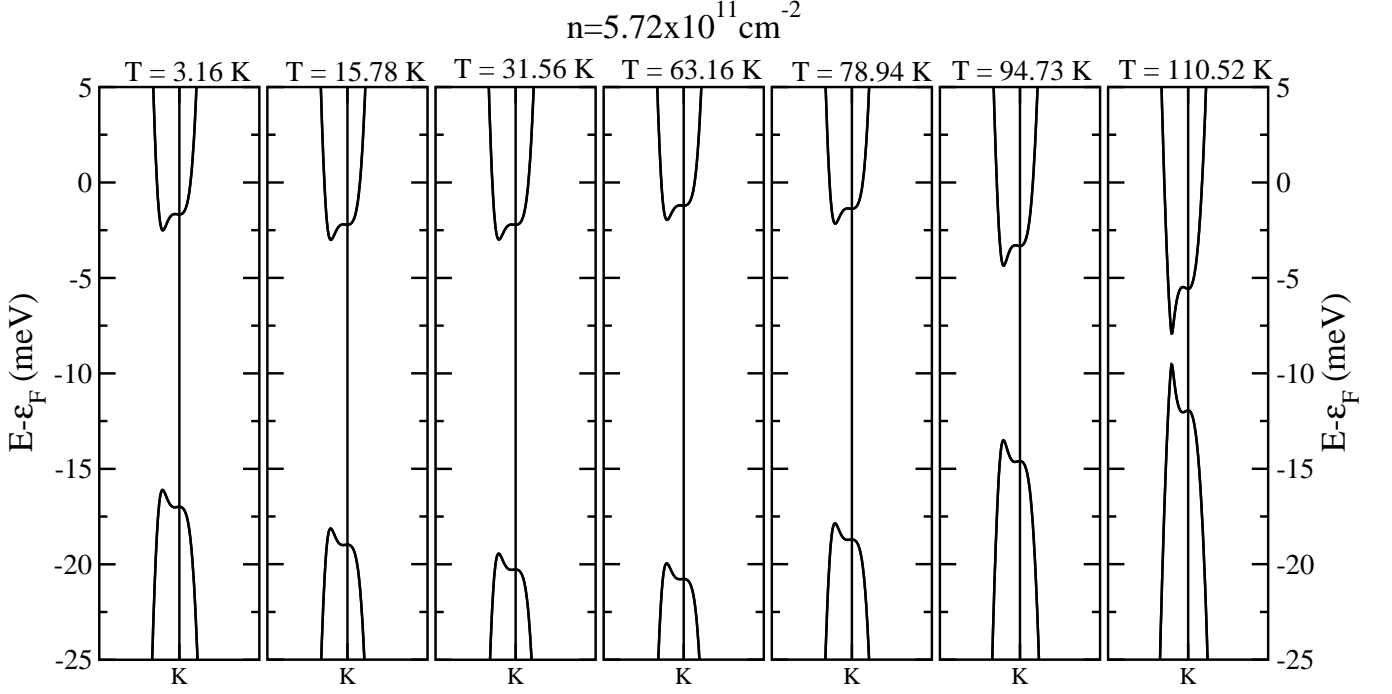


FIG. 10. The electronic band structure of the surface states of the magnetic state of the rhombohedral trilayer graphene at doping $n = 5.72 \times 10^{11} \text{ cm}^{-2}$ for different temperatures. The electronic bands are plotted around 0.035 bohr^{-1} of the \mathbf{K} point along the path $\Gamma \rightarrow \mathbf{K} \rightarrow \mathbf{M}$.

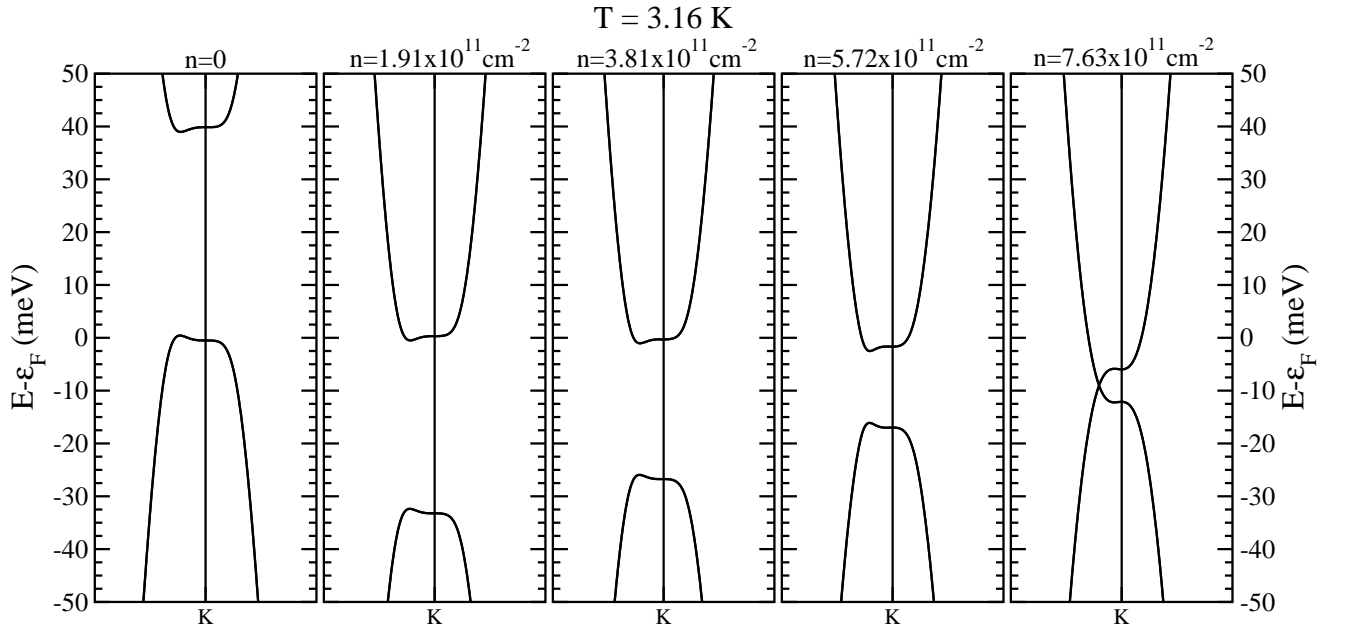


FIG. 11. The electronic band structure of the surface states of the magnetic state of the rhombohedral trilayer graphene at FD smearing temperature $T = 3.16 \text{ K}$ for different doping. The electronic bands are plotted around 0.035 bohr^{-1} of the \mathbf{K} point along the path $\Gamma \rightarrow \mathbf{K} \rightarrow \mathbf{M}$.

electrons/cell (corresponding to the electron density of $n = 1.91 \times 10^{11}, 3.81 \times 10^{11}, 5.72 \times 10^{11}, 7.63 \times 10^{11} \text{ cm}^{-2}$)

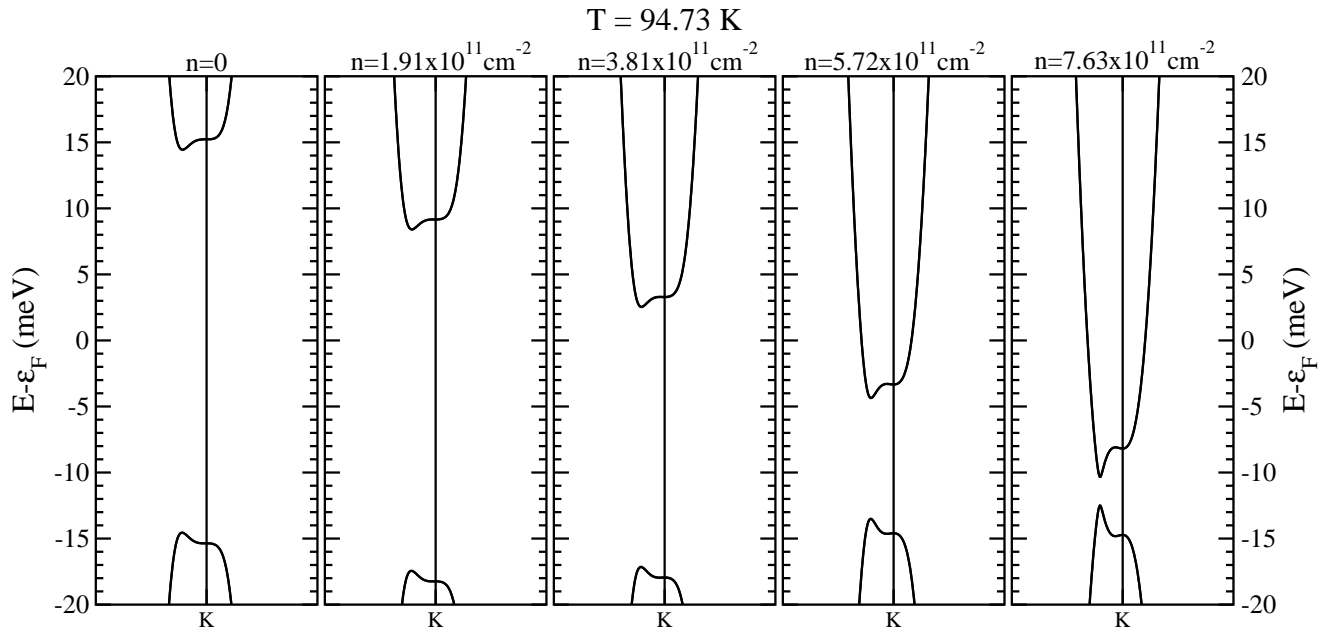


FIG. 12. The electronic band structure of the surface states of the magnetic state of the rhombohedral trilayer graphene at FD smearing temperature $T = 94.73$ K for different doping. The electronic bands are plotted around 0.035 bohr^{-1} of the \mathbf{K} point along the path $\Gamma \rightarrow \mathbf{K} \rightarrow \mathbf{M}$.

to the trilayer rhombohedral graphene. In Fig. 9, we present the temperature dependence of the band gap for different doping, as compared to the undoped case.

With the increasing temperature, after $T \sim 60$ K the band gap decreases sharply, as expected. However, at low temperatures, the band gap first increases. In Fig. 10, we present the electronic structure at doping $n = 5.72 \times 10^{11} \text{ cm}^{-2}$ for different temperatures. In addition, to understand the correlation between the increase in the gap and the spins, we present the spins of each atom at different temperatures for this doping in Table V.

TABLE V. The magnitude of the spin of each atom in $10^{-3} \mu_B$ at each temperature for doping $n = 5.72 \times 10^{11} \text{ cm}^{-2}$.

T (K)	$\mu_1 = -\mu_6$	$\mu_2 = -\mu_5$	$\mu_3 = -\mu_4$
3.16	-1.86	1.62	-1.00
15.78	-2.06	1.79	-1.10
31.56	-2.24	1.95	-1.17
63.16	-2.46	2.14	-1.29
78.94	-2.14	1.86	-1.12
94.73	-1.25	1.09	-0.65
110.52	-0.22	0.19	-0.12

Furthermore, we also present the electronic structure at two different temperatures $T = 3.16$ K and $T = 94.73$ K for different doping in Figs. 11 and 12, respectively. The closing of the band gap with increasing doping is clear from these figures. Also note that the width of the

flat region decreases with increasing doping.

Appendix F: Phonon Modes

TABLE VI. The frequencies in cm^{-1} at the Γ and $\mathbf{K} = \mathbf{K}'$ points of the rhombohedral trilayer graphene.

Γ	\mathbf{K}
0.0000	547.8938
0.0000	547.8938
0.0000	549.8043
19.0449	549.8138
19.0449	555.7702
31.5473	555.7702
31.5473	1011.7181
71.1469	1015.4720
120.6523	1015.4720
762.5849	1192.2007
780.7989	1192.2007
788.6079	1211.2703
1601.4634	1249.0268
1601.4634	1249.1592
1607.1849	1249.3243
1613.3836	1249.3243
1613.3836	1250.3788

We have calculated the phonon modes with the PBE0 functional using a Fermi-Dirac smearing of 0.002 Ha ,

electronic k mesh of $39 \times 39 \times 1$, energy convergence tolerance of 10^{-9} Ha, real space integration tolerances of 7-7-7-15-30, and a $\sqrt{3} \times \sqrt{3} \times 1$ supercell to obtain the modes at both the Γ and K points.

As presented in Table VI, all the phonon modes at the Γ and K points of the Brillouin zone are positive. Therefore, we conclude that there is no charge density wave instability with $\sqrt{3} \times \sqrt{3}$ periodicity to cause the opening of the band gap for this system.

The three phonon modes with a large electron-phonon coupling are at the K point: two degenerate modes at $1192.2007 \text{ cm}^{-1}$ and the other mode at $1211.2703 \text{ cm}^{-1}$. They are softened significantly with the PBE0 functional with exact exchange, as compared to the local density approximation²⁶; however, this softening is not enough to cause an instability. Moreover, this softening is the largest compared to other standard hybrid functionals, since the exact exchange is smaller in the B3LYP and range separation is larger in the HSE06 functional.

-
- * francesco.mauri@uniroma1.it
† matteo.calandra@impmc.upmc.fr
- ¹ F. Freitag, J. Trbovic, M. Weiss, and C. Schönberger, *Phys. Rev. Lett.* **108**, 076602 (2012).
 - ² J. V. Jr, L. Jing, W. Bao, Y. Lee, P. Kratz, V. Aji, M. Bockrath, C. N. Lau, C. Varma, R. Stillwell, D. Smirnov, F. Zhang, J. Jung, and A. H. MacDonald, *Nat. Nano.* **7**, 156 (2012).
 - ³ A. L. Grushina, D.-K. Ki, M. Koshino, A. A. L. Nicolet, C. Faugeras, E. McCann, M. Potemski, and A. F. Morpurgo, *Nat. Comm.* **6**, 6419 (2015).
 - ⁴ M. Koshino, *New Journal of Physics* **15**, 015010 (2013).
 - ⁵ J. Jung and A. H. MacDonald, *Phys. Rev. B* **88**, 075408 (2013).
 - ⁶ S. Latil and L. Henrard, *Phys. Rev. Lett.* **97**, 036803 (2006).
 - ⁷ R. Xiao, F. Tasnádi, K. Koepernik, J. W. F. Venderbos, M. Richter, and M. Taut, *Phys. Rev. B* **84**, 165404 (2011).
 - ⁸ B.-R. Wu, *Applied Physics Letters* **98**, 263107 (2011).
 - ⁹ M. Otani, M. Koshino, Y. Takagi, and S. Okada, *Phys. Rev. B* **81**, 161403 (2010).
 - ¹⁰ D. Pierucci, H. Sediri, M. Hajlaoui, J.-C. Girard, T. Brumme, M. Calandra, E. Velez-Fort, G. Patriarche, M. G. Silly, G. Ferro, V. Souliere, M. Marangolo, F. Sirotti, F. Mauri, and A. Ouerghi, *ACS Nano* **9**, 5432 (2015), pMID: 25893537, <http://dx.doi.org/10.1021/acsnano.5b01239>.
 - ¹¹ Y. Lee, D. Tran, K. Myhro, J. Velasco, N. Gillgren, C. Lau, Y. Barlas, J. Poumirol, D. Smirnov, and F. Guinea, *Nat. Comm.* **5**, 5656 (2014).
 - ¹² W. Bao, L. Jing, J. V. Jr, Y. Lee, G. Liu, D. Tran, B. Standley, M. Aykol, S. B. Cronin, D. Smirnov, M. Koshino, E. McCann, M. Bockrath, and C. N. Lau, *Nat. Phys.* **7**, 948 (2011).
 - ¹³ R. E. Throckmorton and O. Vafek, *Phys. Rev. B* **86**, 115447 (2012).
 - ¹⁴ Y. Henni, H. P. O. Collado, K. Nogajewski, M. R. Molas, G. Usaj, C. A. Balseiro, M. Orlita, M. Potemski, and C. Faugeras, *Nano Letters* **16**, 3710 (2016), pMID: 27164265, <http://dx.doi.org/10.1021/acs.nanolett.6b01041>.
 - ¹⁵ R. Dovesi, R. Orlando, A. Erba, C. M. Zicovich-Wilson, B. Civalleri, S. Casassa, L. Maschio, M. Ferrabone, M. D. L. Pierre, P. D'Arco, Y. Noël, M. Causà, M. Rérat, and B. Kirtman, *Int. J. Quantum Chem.* **114**, 1287 (2014).
 - ¹⁶ M. F. Peintinger, D. V. Oliveira, and T. Bredow, *Journal of Computational Chemistry* **34**, 451 (2013).
 - ¹⁷ C. Adamo and V. Barone, *J. Chem. Phys.* **110**, 6158 (1999).
 - ¹⁸ J. P. Perdew, K. Burke, and M. Ernzerhof, *Phys. Rev. Lett.* **77**, 3865 (1996).
 - ¹⁹ C.-H. Ho, C.-P. Chang, and M.-F. Lin, *Phys. Rev. B* **93**, 075437 (2016).
 - ²⁰ M. Lazzeri, C. Attaccalite, L. Wirtz, and F. Mauri, *Phys. Rev. B* **78**, 081406 (2008).
 - ²¹ A. V. Krukau, O. A. Vydrov, A. F. Izmaylov, and G. E. Scuseria, *J. Chem. Phys.* **125**, 224106 (2006).
 - ²² S. H. Vosko, L. Wilk, and M. Nusair, *Can. J. Phys.* **58**, 1200 (1980).
 - ²³ J.-H. Wong, B.-R. Wu, and M.-F. Lin, *Computer Physics Communications* **182**, 77 (2011).
 - ²⁴ J.-C. Charlier, X. Gonze, and J.-P. Michenaud, *Carbon* **32**, 289 (1994).
 - ²⁵ C.-W. Chiu, Y.-C. Huang, S.-C. Chen, M.-F. Lin, and F.-L. Shyu, *Phys. Chem. Chem. Phys.* **13**, 6036 (2011).
 - ²⁶ J.-A. Yan, W. Y. Ruan, and M. Y. Chou, *Phys. Rev. B* **77**, 125401 (2008).